# 1 Using Rapid Repeat SAR Interferometry to Improve Hydrodynamic Models of Flood

# 2 Propagation in Coastal Wetlands

- 3 Xiaohe Zhang<sup>1\*</sup>, Cathleen E. Jones<sup>2</sup>, Talib Oliver Cabrera<sup>2</sup>, Marc Simard<sup>2</sup>, Sergio Fagherazzi<sup>1</sup>
- <sup>1</sup>Department of Earth and Environment, Boston University, Boston, Massachusetts, USA
- 5 <sup>2</sup>Jet Propulsion Laboratory, California Institute of Technology, Pasadena, California, USA

#### Abstract

The propagation of tides and riverine floodwater in coastal wetlands is controlled by subtle topographic differences and a thick vegetation canopy. High-resolution numerical models have been used in recent years to simulate fluxes across wetlands. However, these models are based on sparse field data that can lead to unreliable results. Here, we utilize high spatial-resolution, rapid repeat interferometric data from the Uninhabited Aerial Vehicle Synthetic Aperture Radar (UAVSAR) to provide a synoptic measurement of sub-canopy water-level change resulting from tide propagation into wetlands. These data are used to constrain crucial model parameters and improve the performance and realism of simulations of the Wax Lake wetlands in coastal Louisiana (USA). A sensitivity analysis shows that the boundary condition of river discharge should be calibrated first, followed by iterative correction of terrain elevation specified originally by a Digital Terrain Model derived from LiDAR measurements. The calibration of bed friction becomes important only with the boundary and topography calibrated. With the model parameters calibrated, the overall Nash-Sutcliffe model efficiency for water-level change increases from 0.15 to 0.53 with the RMSE reduced by 26%. In areas with dense wetland grasses, the LiDAR signal is unable to reach the soil surface, but the L-band UAVSAR instrument detects changes in water levels that can be used to infer the true ground elevation. The high spatial resolution and repeat-acquisition frequency (minutes to hours) observations provided by UAVSAR represent a groundbreaking opportunity for a deeper understanding of the complex hydrodynamics of coastal wetlands.

### **Key points:**

- Uninhabited Aerial Vehicle Synthetic Aperture Radar (UAVSAR) observes large-scale tide propagation beneath vegetation canopies
- UAVSAR observations are used to calibrate tidal flows in wetlands
- Wetland elevation is spatially corrected with calibration of hydrodynamic simulations

### 1. Introduction

30

31

32

33

34

35

36

37

38

39

40

41

42

43

44

45

46

47

48

49

50

51

52

53

54

55

56

Distributary channels in deltaic systems nourish wetlands with flow, sediment and nutrients, contributing to marsh elevation gain and resilience to sea-level rise (Redfield. 1972; Morris et al., 2002; Fagherazzi et al., 2012; FitzGerald and Hughes. 2019; Schuerch et al., 2018). Field observations and modeling have been devoted to understand interactions of flows and sediment transport between channels, tidal flats, and wetlands (Donatelli et al., 2020). Field data have shown that when tidal and riverine waters propagate from channel to vegetation, vegetation increases flow resistance, attenuates waves and increases sediment settling (Reed et al., 1999; Nepf and Vivoni, 2000). The presence of vegetation enhances flows within the channels, which become the main conveyers of water and sediments to the marsh platform (Temmerman et al., 2005). In the Wax Lake Delta in Louisiana (USA), the channel-wetland hydrological connectivity is significant, with 23-54 % of discharge flowing from adjacent channels into wetlands, demanding detailed analyses of wetland hydrodynamics (Hiatt and Passalacqua, 2015). These findings imply complex and nonhomogeneous flow pathways within the vegetation. Despite the importance of collecting hydrodynamic data on the wetland platform, expensive in situ measurements with reduced spatial sampling and resolution hamper progress in modeling flow in complex coastal wetlands. Physics-based numerical models explicitly solve hydrodynamics and sediment transport equations to determine sediment budgets and morphological evolution. Most importantly, numerical models can isolate different driving processes and provide reliable predictions under different scenarios of climate change and sea level rise. For the Wax Lake Delta, numerical model results show that intermediate vegetation height and density are optimal for sediment deposition (Nardin and Edmonds, 2014). Similarly, Oliver et al., (2020) found that the presence of vegetation could increase vertical accretion within vegetation patches but reduce sediment retention within the entire delta. Models can also mimic vegetation establishment, growth, expansion, and mortality and update vegetation parameters in each simulated time-step interactively (Best et al., 2018). The reliability of model results depends on careful calibration of model input parameters, particularly topography and bed roughness, and accurate information of boundary conditions that require synchronous spatial field observations. Often, numerical models of wetlands use Light Detection and Ranging (LiDAR) data to extract the topography of the vegetated area (Zhang et al., 2020), which could lead to a positive bias in elevations due to the incapability of laser of penetrating into the vegetation canopy. This would produce misleading results in marsh models because of the high

sensitivity of marsh species and biomass to subtle topographic differences and inundation depths. LiDAR errors vary spatially as a function of vegetation cover, and a constant correction in elevation cannot capture this spatial complexity. The errors are traditionally categorized by vegetation species and adjusted using point-measurements of RTK and total stations. LiDAR topography can be further refined by relating elevation to aboveground biomass density or using machine-learning methods (Medeiros et al., 2015; Rogers et al., 2018; Cooper et al., 2019). Alizad et al., (2016) calibrated a LiDAR Digital Terrain Model (DTM) of the salt marshes in Apalachicola Bay, Florida, USA, by comparing the biomass distribution obtained from a model to remote sensing data. The modeled biomass was calculated based on the empirical function between biomass and inundation depth put forward by Morris et al. (2002). Model calibration is traditionally based on a few of tidal gauges in large channels, which cannot capture complex flow dynamics within wetlands. The flows on the wetland platform are seldom calibrated due to the challenge of collecting in-situ measurements beneath the vegetation canopy (Alsdorf et al., 2007). Recent advances in the remote sensing of hydraulic variables (e.g. inundation extent and water level), provide an opportunity to fuse high-resolution spatial data into numerical models through calibration (e.g. McCabe et al., 2017; Wiberg et al., 2020). The integration of remote sensing data and numerical models was indicated as one of the grand challenges in salt marsh morphodynamics (Fagherazzi et al., 2020). Spaceborne Interferometry Synthetic Aperture Rader (InSAR) has been successfully applied to estimate water-level changes in wetlands, especially in fluvial systems, because the interferometric phase change of repeat-pass SAR backscattering from emergent flooded vegetation is dominated by the water-level change with a high interferometric coherence (e.g. Alsdorf et al., 2000; Yuan et al., 2015; Oliver-Cabrera & Wdowinski, 2016; Lee et al., 2020; Liao et al., 2020). Based on InSAR-derived water-level change, Jung et al., (2012) calibrated Manning's bed roughness in a 2-D floodplain model of the Atchafalaya River floodplains, reducing the mean absolute error to 5.7 cm in a 64-day simulation. Water levels derived from radar altimetry can be utilized for calibrations of depth and bed roughness in poorly gauged areas (Sun et al., 2012; Domeneghetti et al., 2014). The application of radar altimetry measurements, due to their low accuracy, is limited to large channel systems such as the Amazon River (De Paiva et al., 2013). However, the long temporal repeat of spaceborne InSAR (days to months) inhibits observation of tidal flows into wetlands, and thus cannot be used to calibrate coastal numerical models.

57

58

59

60

61

62

63

64

65

66

67

68

69

70

71

72

73

74

75

76

77

78

79

80

81

Airborne systems such as the Uninhabited Aerial Vehicle Synthetic Aperture Radar (UAVSAR) can fill this gap, providing repeat-pass differential interferometry for water-level changes within 1-hour time window and with high accuracy (e.g. Rosen et al., 2006; Fore et al., 2015). The goal of this paper is to use UAVSAR-derived short timescale water-level change to calibrate hydrodynamic models in tidal wetlands and to assess model sensitivity to boundary conditions, LiDAR-derived topography and bed roughness. To this end, we develop a 2-D Delft3D hydro-model with high-spatial resolution (~ 10 m), covering the Wax Lake Delta and adjacent wetlands. We focus our calibration effort in the western wetland area dissected by meandering channels (Fig. 1). The work presented here introduces a novel approach to integrate airborne InSAR observations into quantitative models of tidal flow propagation in coastal vegetated surfaces.

### 2. Study site

The Wax Lake Delta is a river-dominated delta located in the Atchafalaya Bay within the greater Mississippi River Delta. The Atchafalaya River distributes water and sediment into Atchafalaya Bay through the Wax Lake Outlet, artificially dredged in 1942. The sediment has in time formed the Wax Lake Delta (Robert et al., 2015; Shaw et al., 2013). The delta is about 20 km from the Calumet Gauge (USGS 07381590), and the width of main channel is ~300 m (Fig. 1A).

The low-lying Atchafalaya Bay is affected by a mixed semidiurnal micro-tide, with the mean tidal range of 0.34 m. The river discharge varies seasonally from 2500 m³/s to more than 5000 m³/s during river floods. A portion of discharge is diverted along the engineered Gulf Intercostal Waterway (GIWW) that crosses the Wax Lake Outlet (Swarzenski and Perrien 2015). Extensive heterogeneous plant communities have developed along the two sides of the main channel. A dendritic network of meandering channels departing form the main stem brings water and sediment to these vegetated areas. Here we focus on Wax Lake (WL) channel and Hog Bayou (HB) channel in the western side of the main channel (Fig. 1B). Most research in the Wax Lake Delta focuses on mechanisms controlling the naturally prograding delta itself, without considering the role of these large-scale wetlands in modulating water and sediment inputs (Carle et al., 2015; Oliver et al., 2020).

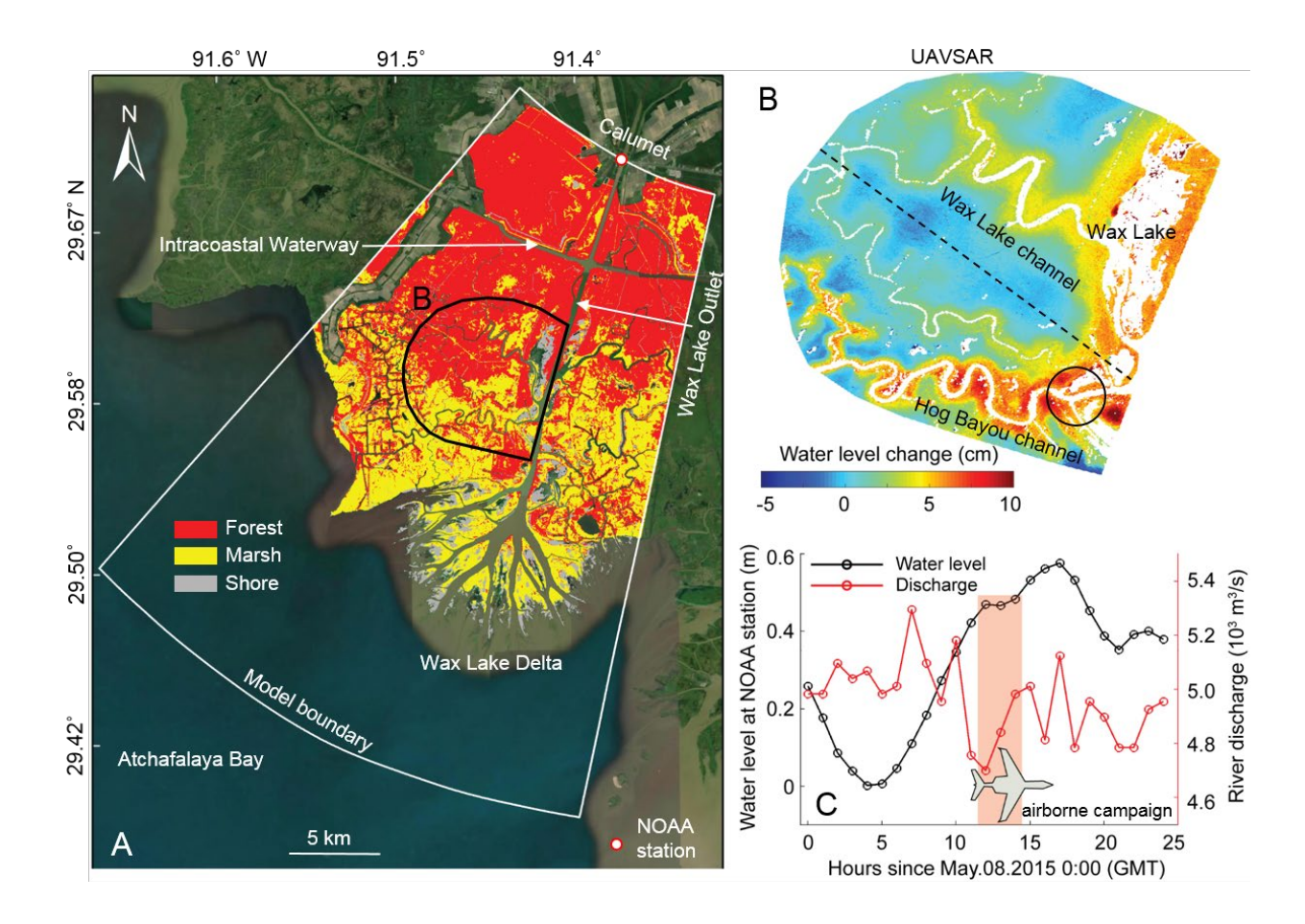


Figure 1. (A) A 10-m resolution vegetation classification map based on Sentinel-2 satellite imagery (Thomas et al., 2019) within the Wax Lake Delta model boundary (white line). The area within black line is the domain used for comparison with model results and visualization purpose. (B) Cumulative water-level change observed by UAVSAR from 11:34 to 13:53 (GMT) on 08 May 2015. The system is divided by the dashed line in the upper subdomain of Wax Lake channel (WL) and the lower subdomain of Hog Bayou channel (HB). The black circle indicates the inlet area of HB channel. (C) Field observations of water levels (NOAA Amerada Pass 8764227) and river discharge (USGS Calumet 07381590) on 08 May 2020. The pink band indicates the period of the airborne campaign.

### 3. Methods

### 3.1 UAVSAR Interferometry

UAVSAR is a fully polarimetric (quad-polarization) L-band (wavelength  $\lambda$ =0.2379 m, frequency v=1.257 GHz) synthetic aperture radar operated by the U.S. National Aeronautics and Space Administration (NASA) and deployed

on a Gulfstream-3 aircraft. The system is designed for both polarimetry (PolSAR) and repeat-pass interferometry (InSAR) (Hensley et al, 2003). InSAR processing of repeated observations of a surface from a same viewing geometry enables measurement of surface displacement in the line-of-sight direction (Rosen et al., 2006). Because the instrument is side looking, the line-of-sight displacement is in general a combination of vertical and horizontal displacements. Relating the measured displacement to a change in surface elevation requires knowledge of the horizontal displacement, through either measurement or ancillary information. In flooded wetlands, the backscattered signal is primarily due to double bounce scattering from the water and vegetation, so the measured surface displacement is due to change in water level (Lu and Kwoun, 2008; Wdowinski et al., 2013; Liao et al., 2019). This study uses repeat-pass UAVSAR data (6 m spatial resolution) acquired in HH polarization mode (Horizontal transmit and receive) to measure the net change in water level between 11:34 and 13:53 (GMT) on 08 May 2015. The measured interferometric phase change,  $\Delta \varphi$ , is converted to elevation change,  $\Delta z$ , by first phase unwrapping to remove the  $2\pi$ ambiguities (Chen and Zebker, 2002), converting the unwrapped phase,  $\Delta\Phi$ , to line-of-sight displacement,  $\Delta = \Delta\Phi\lambda/4\pi$ , then projecting the value into the vertical direction,  $\Delta z = \Delta l/\cos(\theta)$ , using the incidence angle,  $\theta$ . The errors of surface deformation can be controlled within 1 cm for repeat pass SAR observations within hours, making it well suited for imaging water-level changes in coastal wetlands (Rosen et al., 2006). More details about UAVSAR-derived water level change maps can refer to Jones et al., (2020) (https://doi.org/10.3334/ORNLDAAC/1823).

137

138

139

140

141

142

143

144

145

146

147

121

122

123

124

125

126

127

128

129

130

131

132

133

134

135

136

### 3.2 Hydrodynamic modelling setup

A 2-D hydrodynamic model based on Delft3D was developed to solve flow dynamics. The model domain is a curvilinear grid of 2600 by 1700 cells, with the size ranging from 100 m<sup>2</sup> to 150 m<sup>2</sup> in the area of wetlands (Figs. 2B, 2C). The model topography is a 10-m seamless DTM composed of LiDAR datasets (<a href="http://ned.usgs.gov/">http://ned.usgs.gov/</a>), sonar transects in channels, and bathymetry elevations derived from diverse source data referred to the NAVD88 vertical datum (Denbina et al., 2020). We specify river discharge at the Calumet Gauge station (USGS 07381590) (U.S. Geological Survey. 2016) as the upstream boundary, and tidal water levels at the NOAA Amerada Pass station (NOAA 8764227) (CO-OPS 2018) as the ocean boundary (Fig. 2A). The hourly wind speed (~ 3 m/s) and direction measured at this NOAA station are uniformly prescribed across the model domain to account for the influence of winds on hydrodynamics.

Bed roughness is defined based on a 10-m Sentinel-2 classification map (Thomas et al., 2019) and a look-up table for the Chezy's coefficient: ocean (60 m $^{1/2}$ /s), channel water (55 m $^{1/2}$ /s), shoals (45 m $^{1/2}$ /s), marsh (35 m $^{1/2}$ /s) and forest (8 m $^{1/2}$ /s) (Chow, 1959; Straatsma and Baptist, 2008). The threshold depth for wetting and drying is set as 0.001 m to keep model stability for very shallow waters. The simulation period is from 05 May 2015 at 00:00 to 09 May 2015 at 00:00, and a time step of 0.2 min is adopted to satisfy all stability criteria for the parallel computation.

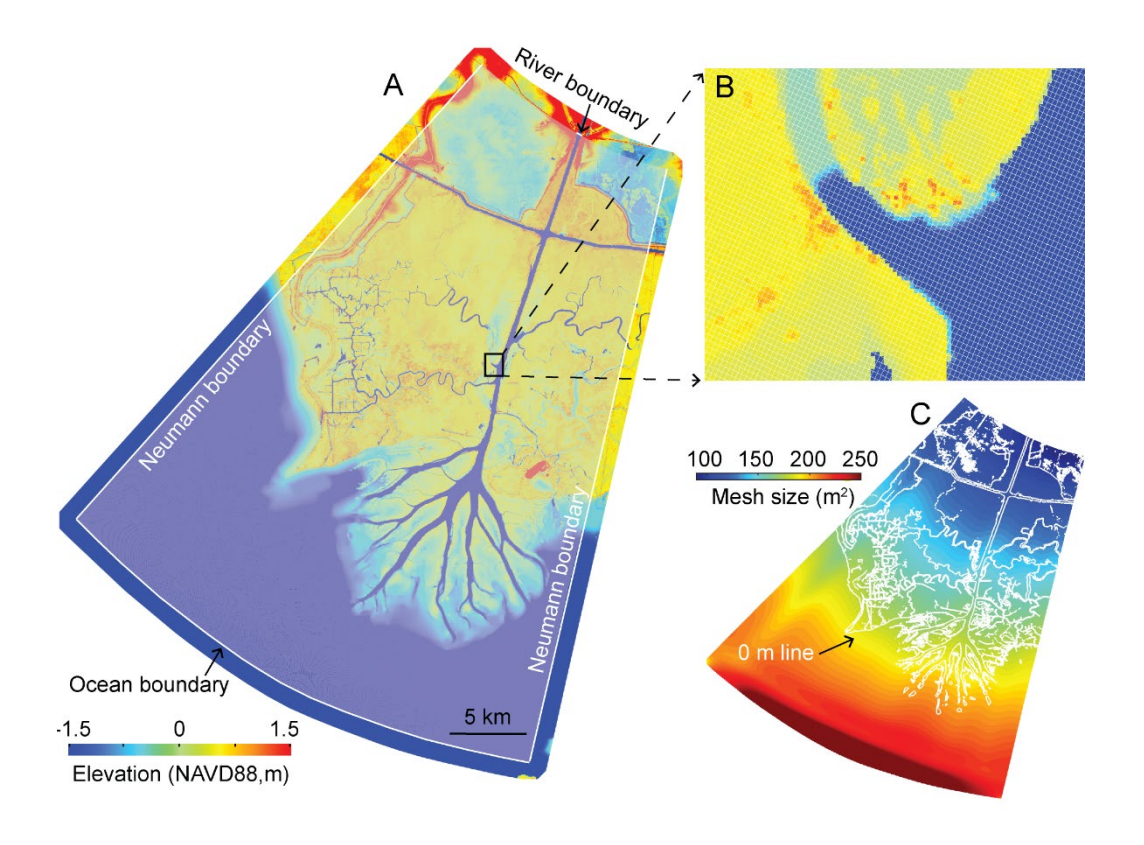


Figure 2. (A) Model boundaries setup and elevation data as base map. (B) Zoomed map at Wax Lake channel inlet for mesh visualization. (C) Map of mesh size.

The analysis is focused within the western wetland (Fig. 1B) in a 2.5-hour window on May 08 from 11:34 to 13:53 when the UAVSAR data were collected. This time window corresponds to spring high tides and river floods, thus is optimal for water level observations over the wetlands. The Nash-Sutcliffe model efficiency (ME), root mean square error (RMSE), and frequency curve of difference between model (M) and remote sensing data (D) are used to evaluate model performance:

161 
$$ME = 1 - \frac{\sum (D-M)^2}{\sum (D-\overline{D})^2}$$
, RMSE =  $\sqrt{\sum \frac{(D-M)^2}{n}}$  (1)

where n is the number of observations, and  $\overline{D}$  is the mean of n values. The value of ME represents the model performance: ME > 0.65 excellent; 0.5 < ME < 0.65 very good; 0.2 < ME < 0.5 good; and ME < 0.2 poor (Allen et al., 2007).

3.3 Calibration and validation of river discharge and wetland elevation

162

163

164

165

166

167

168

169

170

171

172

173

174

175

176

177

178

179

180

181

182

183

184

185

186

187

The riverine flow from the Wax Lake Outlet debouches seaward crossing the Intercostal Waterway (Fig. 1A). The GIWW likely modifies the discharge entering the Wax Lake delta and the lower wetlands. As river flows can attenuate tidal propagation, reducing temporal variations in water level (Sassi and Hoitink, 2013), the river discharge at the model boundary should be adjusted to account for the discharge diverted in the GIWW. No synchronous discharge data from USGS is available along the GIWW at the period of the UAVSAR measurements. We therefore validate the discharge adjustment based on an empirical calculation using water surface slope data derived from remote sensing. The calibration of the model is performed in two steps (Fig. 3). First, we calibrate the river discharge to match UAVSAR data at the wetland margins bordering the Wax Lake Outlet (Section 3.2); we then spatially modify the wetland topography in each cell (Section 3.3) by adding the difference between water-level change estimated by the model and the UAVSAR observations. If the UAVSAR change is larger than the model result, we decrease the elevation of that cell. The model is iteratively re-run with the new bathymetry until the elevation correction is negligible and ME and RMSE are near-constant. The elevation correction is necessary for two reasons: 1) marsh topography derived from LiDAR data is prone to errors, because the laser signal cannot penetrate the thick vegetation resulting in an error (see Rosso et al. 2006). This offset is very high for a wetland that is typically submerged by only few tens of centimeters at high tide, precluding water flow in several areas. 2) a simple adjustment of local friction would not be able to correct for the error, and would lead to unrealistic friction values. The correction in elevation proposed here is empirical, and based on the assumption that lowering the bed elevation would likely allows for more tidal propagation and for spreading out the water level changes. In facts water level changes are affected by flow conveyance. To achieve a large change in water depth you need to increase flow

conveyance which can be done by increasing water depth. Note that a change in elevation at one point would

reverberate across the system, changing the flow conveyance along the entire flow path. To address this shortcoming,

we decided to iteratively change the elevation of a small amount, so that the entire system can slowly adjust to the modification in conveyance. This method is effective only if the iteratively procedure converges, and only if the final result is realistic (i.e. the system does not present multiple equilibrium points). Here, for simplicity, we chose to modify the elevation by the change in elevation measured by UAVSAR in 2.5 hr. This choice was arbitrary, and a smaller change in elevation (e.g. change in elevation measured by UAVSAR in 1 hr) would lead to similar results after several iterations.

Finally, the sensitivity of the results to the friction coefficient for the marsh and forest surfaces is evaluated. We designed 49 scenarios with 7 different friction values (Chézy coefficient) ranging from 8 m<sup>1/2</sup>/s to 40 m<sup>1/2</sup>/s for the marsh and forest respectively, and launch models with different combinations of frictions before and after the calibration of river discharge and topography.

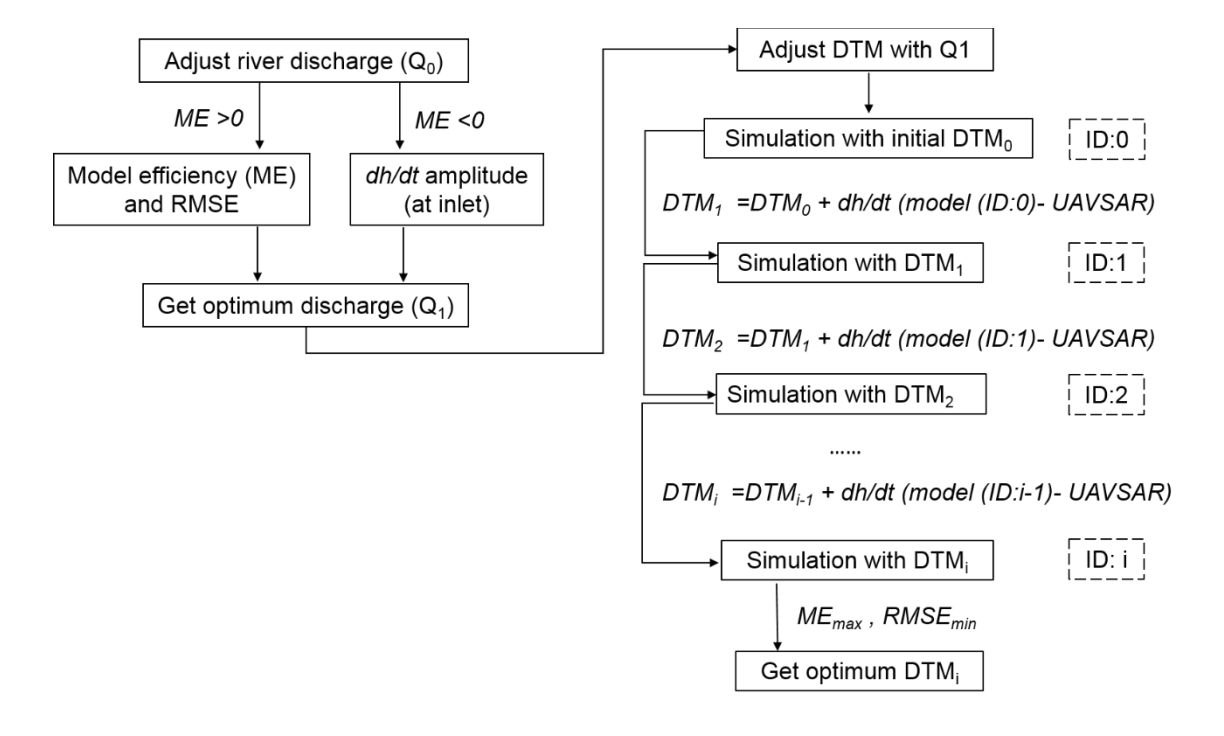


Figure 3. Flow diagram of model calibration process using UAVSAR data

The computed river discharge is validated using the empirical Manning's equation that estimates flow rate in open channels as a function of water level slope, channel cross section, and bed friction (Chow, 1959):

$$202 Q = ACR_h^{1/2}S^{1/2} (2)$$

Where Q is flow discharge (m<sup>3</sup>/s), A is channel cross section (m<sup>2</sup>), C is Chézy bed roughness (m<sup>1/2</sup>/s),  $R_h$  is hydraulic radius (m), S is the water channel slope. The Manning equation is applied to two cross sections of the Wax

Lake outlet: one before the intersection with the GIWW (cross section a-a' in Fig. 4) and one after (cross section b-b'

206 in Fig. 4):

203

204

205

211

212

213

$$207 \qquad \frac{Q_2}{Q_1} = \frac{A_2}{A_1} \frac{C_2}{C_1} \left(\frac{R_{h2}}{R_{h1}}\right)^{1/2} \left(\frac{S_2}{S_1}\right)^{1/2} \tag{3}$$

Where subscript 1 refers to cross section a-a', subscript 2 refers to b-b'. We thus obtain the value,  $Q_2$ , of the discharge

after the GIWW that can be compared to the calibrated discharge.

The channel slope in Eq. 3 is derived from AirSWOT data (Denbina., 2019). AirSWOT is an airborne Ka-band

synthetic aperture radar that measures water surface elevation in open waters with uncertainty below 0.3 cm/km. The

AirSWOT campaign was conducted at 17:14 (GMT) on 09 May 2015, and more details about the AirSWOT

measurements can be found in Denbina et al., (2021). The comparison allows quantifying the effect of the GIWW on

river discharge.

215 The new wetland elevations obtained with our method are validated with high-resolution elevation data at 10 long-

term sites of the Coastwide Reference Monitoring System (CRMS, https://lacoast.gov/crms/, see locations in Fig.4).

Only four of these sites fall within the UAVSAR footprint, and can therefore be used for the validation.

218

219

220

216

217

### 4. Results

4.1 Tidal propagation beneath vegetation canopies observed by UAVSAR

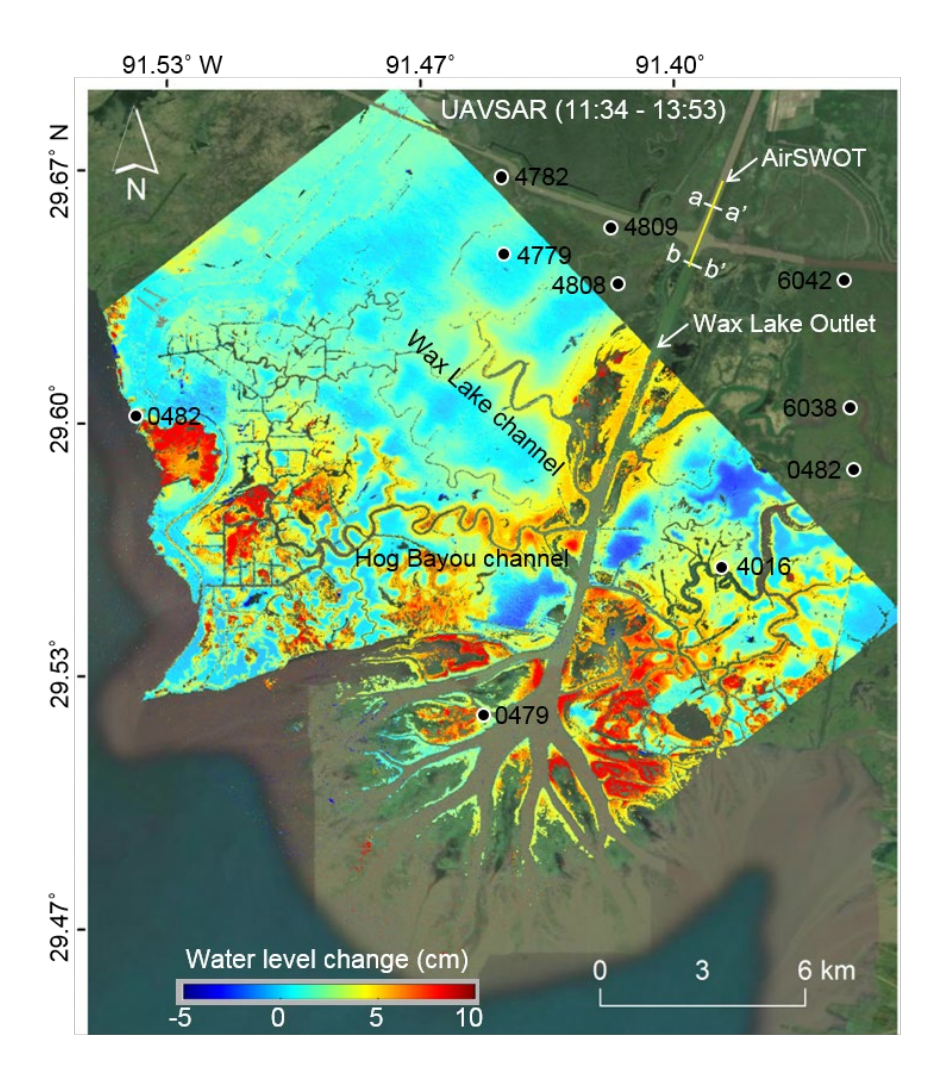


Figure 4. Water level changes observed by UAVSAR between 11:34 and 13:53 (GMT) on 08 May 2015. The location of AirSWOT water surface elevation measurements is also indicated, as well as the Coastwide Reference Monitoring System (CRMS) sites and the cross sections a-a' and b-b'.

UAVSAR observed water level changes below vegetation canopies across the model domain in a 2.5-hour time window (Fig. 4). Changes in water levels are lower in the wetland interior, due to tidal propagation, dissipation and reduced hydraulic connectivity. The zone with more pronounced flooding (large change in water level) extends about 8-10 km from the Wax Lake Outlet mainly to wetlands along the channels, with a width of 200-300 m at both sides of

Interestingly, the HB channel has a width similar to the upper WL channel, but features higher water level variations.

each channel. UAVSAR cannot measure water level change in unvegetated areas, such as ponds and channels (Fig. 4).

There is no clear spatial pattern of water level variations in different vegetation covers (see Fig. 1A and Fig. 4).

## 4.2 River discharge dominates the amplitude of water-level change

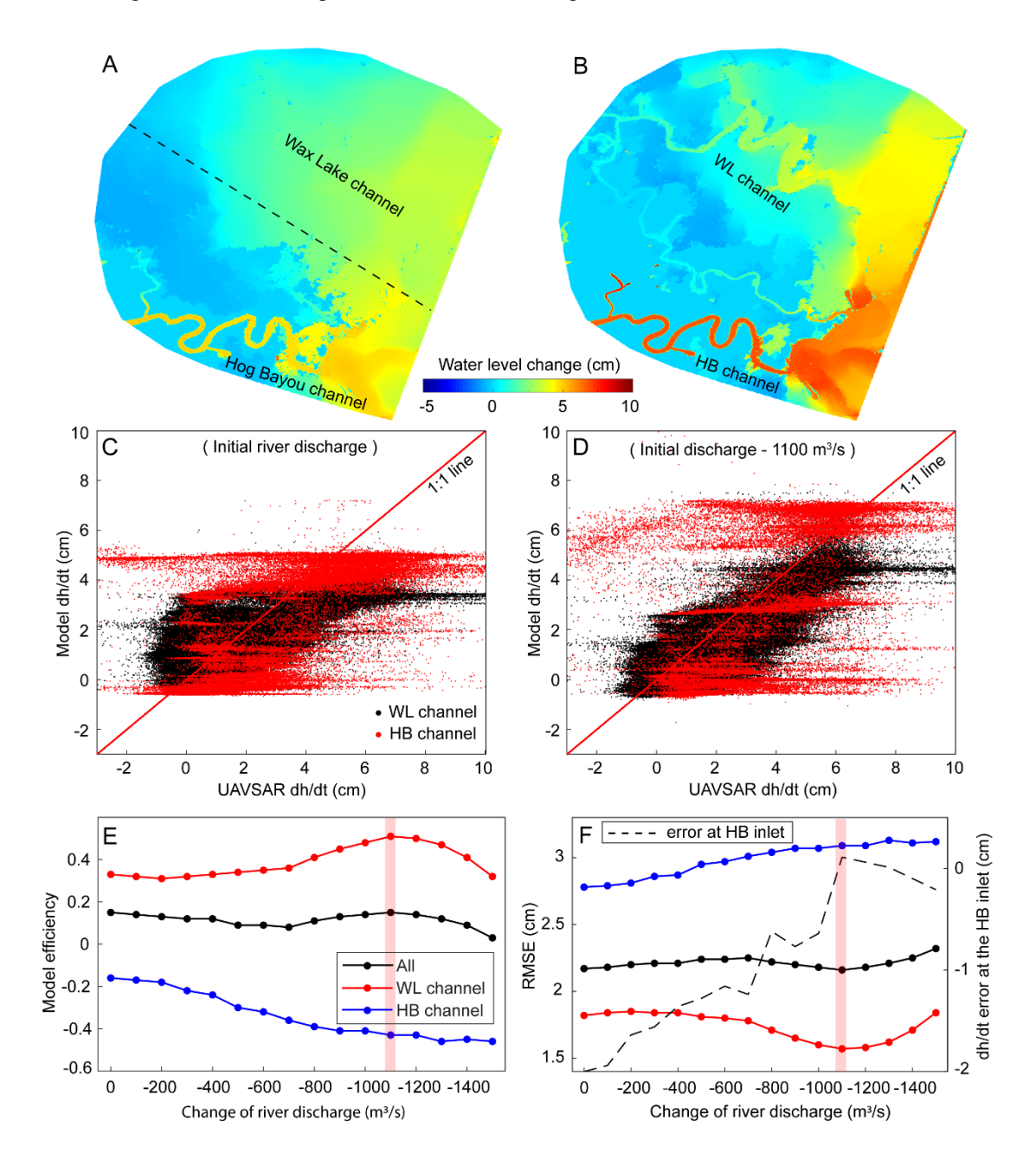


Figure 5. Comparison of model results before and after the correction of river discharge. Spatial distribution of modeled water-level changes with (A) initial river discharge measured at USGS Calumet Gauge (Fig. 1C) and (B) a river discharge reduced by 1100 m<sup>3</sup>/s. (C,D) Comparison of water-level changes between model results and UAVSAR data for the entire domain (area shown in A). (E) Model efficiency (negative value indicates very poor performance

239	that is less meaningful) and (F) RMSE with different river discharges for the entire domain, and for the subdomains
240	of Wax Lake channel (WL) and Hog Bayou channel (HB), separated by the dashed line in (A). Dash line in (F) is the
241	error (model-UAVSAR) of the averaged water-level change (dh/dt) at the inlet of the HB channel (black circle in Fig.
242	1B). The pink band indicates the optimum river discharge adopted after calibration.
243	Our model results show that imposing the river discharge measured at Calumet in the WL channel underestimates
244	tide-induced water-level changes along the HB channel. The use of the discharge measured at the Calumet station as
245	the northern boundary condition gives rise to a uniform flow within the wetlands fed by the WL channel (Fig. 5A), in
246	disagreement with the UAVSAR observations (Fig. 1B), resulting in poor model performance (Fig. 5C). By lowering
247	river discharge, the tidal signal becomes more important and yields a distribution of water level variations comparable
248	to UAVSAR observations, especially in the HB channel (Figs. 5B, 5D). Generally, we find that a lower river discharge
249	gives better results in the subdomain of the WL channel, increases ME from 0.33 to 0.51, and reduces the RMSE from
250	1.82 cm to 1.57 cm (Figs. 5E, 5F). A reduced river discharge in the WL channel is likely caused by the intracoastal
251	waterway, that captures part of the river flow.
252	Since the RMSE is meaningless with negative values of ME (Eqs.1), we used the averaged value of water-level
253	changes at the inlet of the HB channel for calibration (Fig. 1B). The difference between water level change estimates
254	by the model and the UAVSAR observations decreases with reduced river discharges (Fig. 5F). Overall, the optimum
255	river discharge (initial discharge – 1100 m³/s, about 20 % reduction in river discharge) was determined by evaluation
256	of ME, RMSE and regional water-level changes. A flow diversion of 1100 m³/s in the GIWW is in accordance with
257	the average discharge of 800 m <sup>3</sup> /s measured during peak flows by USGS (Swarzenski and Perrien 2015).

4.3 Iterative modification of LiDAR-derived topography

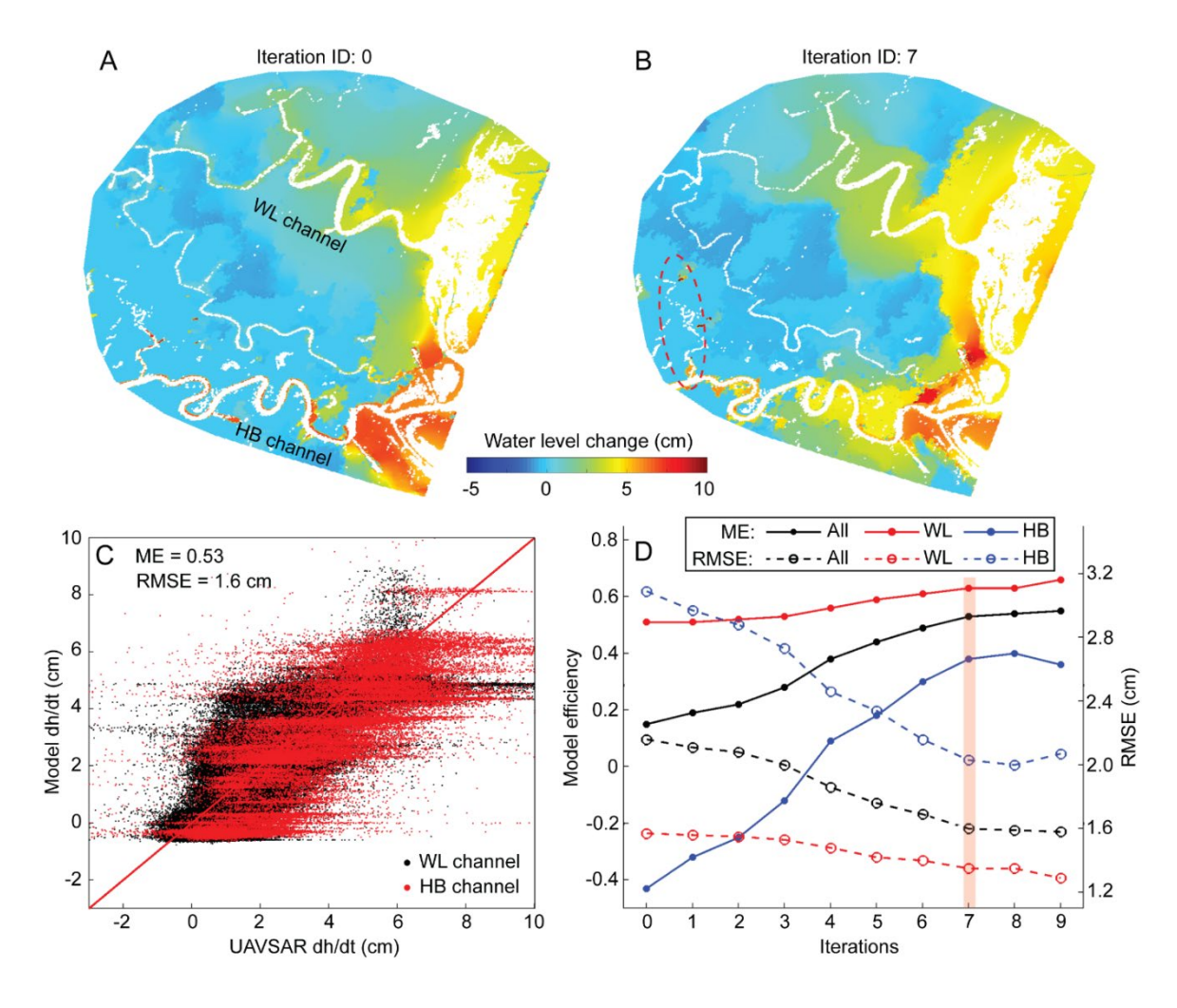


Figure 6. Modeled water-level changes on the wetland surface using Calumet discharge minus 1100 m3/s with (A) original DTM and (B) modified DTM after 7 iterations. DTM in (i+1) iteration = DTM in (i) iteration + difference of water-level changes between model run in iteration (i) and UAVSAR data. (C) Modeled results as a function of UAVSAR data for the entire domain. (D) Model efficiency and RMSE as a function of iteration number for the entire domain (same domain as A), subdomains of Wax Lake channel (WL) and Hog Bayou channel (HB). The pink band indicates the optimum scenario adopted after 7 iterations.

Despite the improvement in the magnitude of water-level changes at the wetland margin after calibrating the river discharge (Fig. 5), the model does not accurately capture tidal propagation on the wetland platform (Fig. 6A). This is probably caused by errors in the LiDAR-derived topography due to the inability of the laser to penetrate a dense canopy (Hladik and Alber. 2012). According to the Delta-X project datasets (https://deltax.jpl.nasa.gov/), the LiDAR DTM may have biases of 20 cm and RMSE of 24 cm in the Wax Lake Delta, which can significantly impact reliability

of hydrodynamic models of coastal wetlands, particularly in microtidal systems (Alizad et al., 2020). Instead of correcting the topography using limited RTK-GPS points, we introduce an approach based on the coupling of UAVSAR observations with model simulations to iteratively correct the model DTM. The correction is different at every point in the domain.

Specifically, we iteratively change the initial DTM by subtracting the difference between the modeled and UAVSAR-observed water-level change. After each modification (iteration) of the DTM, the model is re-run with the updated DTM until the topography converges to the optimum scenario with tidal propagation and dissipation occurring in the wetland interior. The final model results are more realistic, and compare well to UAVSAR observations (Figs. 6A, 6B). The improvement is especially evident in the HB subdomain (Fig. 6C and Fig. 5D). The model performance increases after each iteration, and the DTM at iteration 7 is chosen as the optimum scenario given insignificant improvements in overall domain ME and RMSE in later iterations (Fig. 6D). Overall, the water-level change ME increased from 0.15 to 0.53 after 7 iterations, while the RMSE decreased from 2.16 cm to 1.60 cm; for the WL channel subdomain, the ME improved from 0.51 to 0.63 with RMSE decreasing from 1.57 cm to 1.35 cm; for the HB channel subdomain, the ME improved from -0.52 to 0.22, while the RMSE decreased from 3.14 cm to 2.25 cm. The lower ME value in the HB channel is mainly caused by the spatial resolution of the model which is too low to capture tidal propagation within the small-scale creeks at the end of the domain (dash red circle in Fig. 6B). Ignoring the area near the small-scale creeks improves ME from 0.22 to 0.38 and RMSE from 2.25 cm to 2.03 cm.

The DTM correction varies in space and is generally larger along the channel margins (Fig. 7B). The change is about 0.1 m in the WL channel but can reach 0.4 m along the HB channel (positive value indicates a lowering of the elevation). The modified DTM gives a lower elevation in general, as expected when the LiDAR pulses do not reach the ground in the presence of dense vegetation. High-density marshes in the HB channel may cause the higher bias compared to the forested banks of the WL channel (Fig. 1A). After the river discharge calibration and subsequent DTM correction based on UAVSAR measurements, the distribution of the error between model and UAVSAR is more symmetrical and with the centroid shifting toward zero (Fig. 7C).

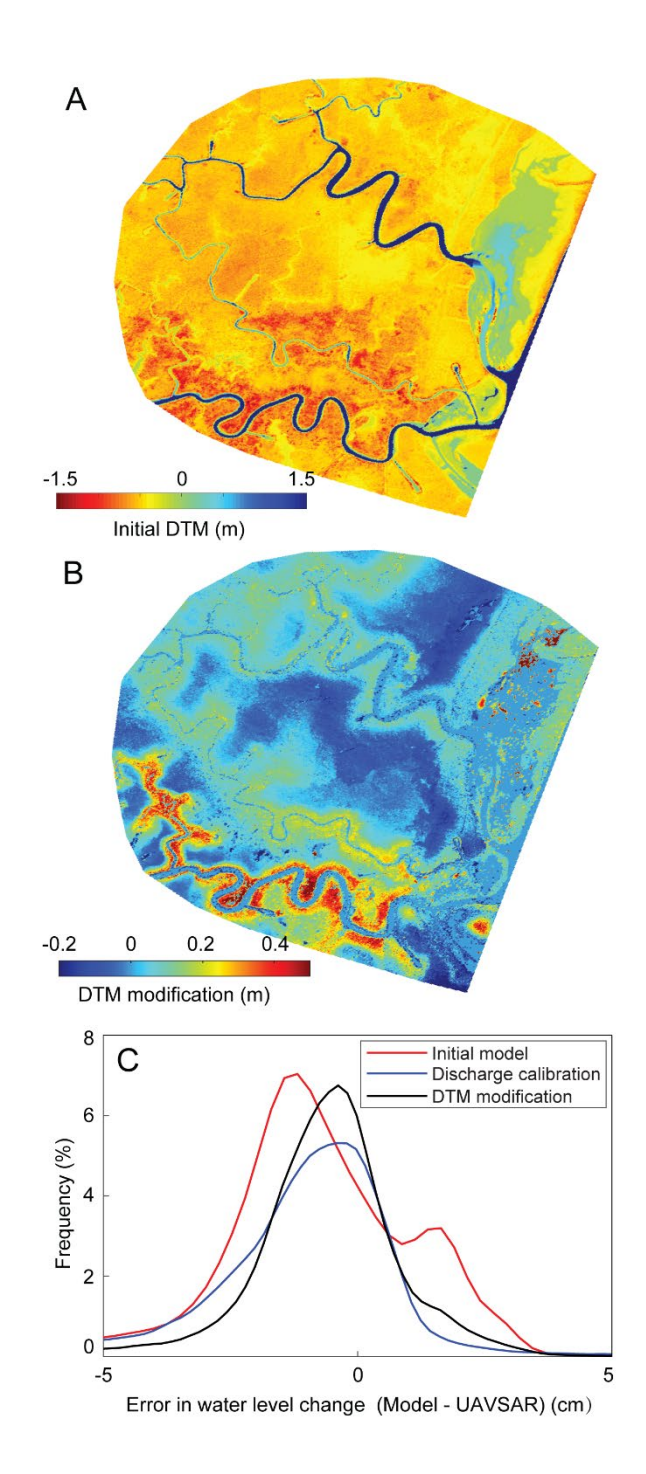


Figure 7. (A) Initial DTM (elevations referred to NAVD 88). (B) Difference in DTM elevation after UAVSAR correction: positive values indicate a lower elevation. (C) Distribution of the error between model and UAVSAR data for: initial model (Fig. 5A), after calibration of river discharge (Fig. 5B), and spatial modification of DTM (Fig. 6B).

With initial river discharge and topography, the calibration of bed friction for the marsh and forest little improved the model performance in terms of ME and RMSE (Tables 1, 2). The forest friction dominates the ME, with less friction (larger Chézy coefficient) in the forest decreasing the overall model performance (Table 1). The ME is weakly related to variations in friction coefficients. For instance, model results with the friction combination (marsh:  $35 \text{ m}^{1/2}/\text{s}$ , forest:  $8 \text{ m}^{1/2}/\text{s}$ ) display same ME and RMSE values as the case (marsh:  $35 \text{ m}^{1/2}/\text{s}$ , forest:  $25 \text{ m}^{1/2}/\text{s}$ ). Overall, a ME < 0.2 in all simulations indicate a poor model performance (Allen et al., 2007). Therefore, the calibration in bed frictions is less meaningful without a careful calibration of boundary conditions (river discharge) and initial conditions (topography).

After modifications of river discharge and topography, the model performance improves (Tables 3, 4). It is interesting to note that the model with friction scenario (marsh: 35 m<sup>1/2</sup>/s, forest: 8 m<sup>1/2</sup>/s) performs best, achieving the highest ME. This is probably because we calibrated river discharge and topography with these friction values. The modified topography therefore retains information about the friction distribution, optimizing the model results. The sensitivity analysis (Table 3) shows the ME ranges from 0.38 to 0.53, and RMSE from 1.6 cm to 1.85 cm. Therefore, the influence of the friction coefficients on model results increases, and becomes important only after calibration of river discharge and DTM elevation.

To shed more light on the effect of friction, we compare two scenarios against the final model calibration by increasing marsh roughness (marsh: 8 m<sup>1/2</sup>/s, forest: 8 m<sup>1/2</sup>/s) and decreasing forest roughness (marsh: 35 m<sup>1/2</sup>/s, forest: 35 m<sup>1/2</sup>/s) (Fig. 8). The watershed of the HB channel is characterized by salt marshes, and more friction in the marsh constrains flows in the channel, increasing variations in water levels along the channel banks (Fig. 8a). With a lower friction in the forest, variations in water levels decrease near the WL channel but increase farther away (Fig. 8c). Both scenarios lower the model performance compared to the initial bed friction scenario (Fig. 8b).

Table 1. Model efficiency for 49 scenarios of bed friction for marsh and forest surfaces before calibration of discharge and DTM. Pink color indicates Chézy marsh values ≥ forest values.

Model Efficiency before calibration of discharge and DTM									
Marsh (Chézy friction)									
$\lim_{s \to \infty} \frac{1}{\sqrt{2}} \cdot \frac{(m^{1/2}/s)}{s}$	8	15	20	25	30	35	40		
For (Ch.	0.16	0.17	0.17	0.16	0.16	0.16	0.16		

15	0.11	0.13	0.14	0.15	0.15	0.14	0.14
20	0.08	0.11	0.12	0.12	0.12	0.12	0.12
25	0.05	0.08	0.1	0.12	0.15	0.16	0.16
30	0.18	0.18	0.16	0.14	0.11	0.08	0
35	0.07	-0.02	-0.06	-0.06	-0.08	-0.12	-0.16
40	-0.02	-0.1	0.14 0.12 0.1 0.16 -0.06 -0.13	-0.14	-0.17	-0.22	-0.22

Table 2. Root-Mean-Square Error for 49 scenarios of bed friction for marsh and forest surfaces before calibration of discharge and DTM. Pink color indicates Chézy marsh values  $\geq$  forest values.

RMSE before calibration of discharge and DTM								
			Ma	rsh (Chézy	friction)			
	(cm)	8	15	20	25	30	35	40
(Chézy friction)	8	2.15	2.15	2.14	2.15	2.15	2.15	2.16
	15	2.22	2.19	2.18	2.17	2.17	2.18	2.18
	20	2.26	2.22	2.21	2.2	2.21	2.21	2.21
Ché	25	2.29	2.26	2.23	2.21	2.17	2.15	2.15
	30	2.13	2.13	2.16	2.18	2.22	2.25	2.35
Forest	35	2.27	2.38	2.42	2.43	2.45	2.48	2.53
	40	2.37	2.47	2.5	2.52	2.54	2.59	2.6

Table 3. Table 1. Model efficiency for 49 scenarios of bed friction for marsh and forest surfaces after calibration of discharge and DTM. Pink color indicates Chézy marsh values ≥ forest values.

Model Efficiency after calibration of discharge and DTM									
	Marsh (Chézy friction)								
	$(m^{1/2}/s)$	8	15	20	25	30	35	40	
Forest (Chézy friction)	8	0.44	0.5	0.49	0.49	0.51	0.53	0.52	
	15	0.46	0.46	0.45	0.43	0.44	0.44	0.46	
	20	0.4	0.45	0.48	0.48	0.45	0.48	0.45	
Ché	25	0.46	0.43	0.43	0.48	0.45	0.45	0.45	
est (	30	0.47	0.44	0.42	0.41	0.4	0.38	0.37	
For	35	0.4	0.37	0.36	0.35	0.34	0.33	0.33	
	40	0.37	0.35	0.33	0.33	0.32	0.32	0.31	

Table 4. Root-Mean-Square Error for 49 scenarios of bed friction for marsh and forest surfaces after calibration of discharge and DTM. Pink color indicates Chézy marsh values ≥ forest values.

	RMSE after calibration of discharge and DTM									
Marsh (Chézy friction)										
	(cm)	8	15	20	25	30	35	40		
Forest (Chézy friction)	8	1.76	1.66	1.68	1.68	1.65	1.6	1.63		
	15	1.73	1.74	1.75	1.77	1.76	1.76	1.72		
zy f	20	1.82	1.75	1.7	1.7	1.74	1.7	1.75		
Ché	25	1.73	1.78	1.77	1.7	1.74	1.75	1.74		
est (	30	1.72	1.77	1.79	1.8	1.82	1.85	1.87		
For	35	1.82	1.87	1.89	1.9	1.91	1.92	1.93		
	40	1.87	1.9	1.92	1.93	1.94	1.94	1.95		



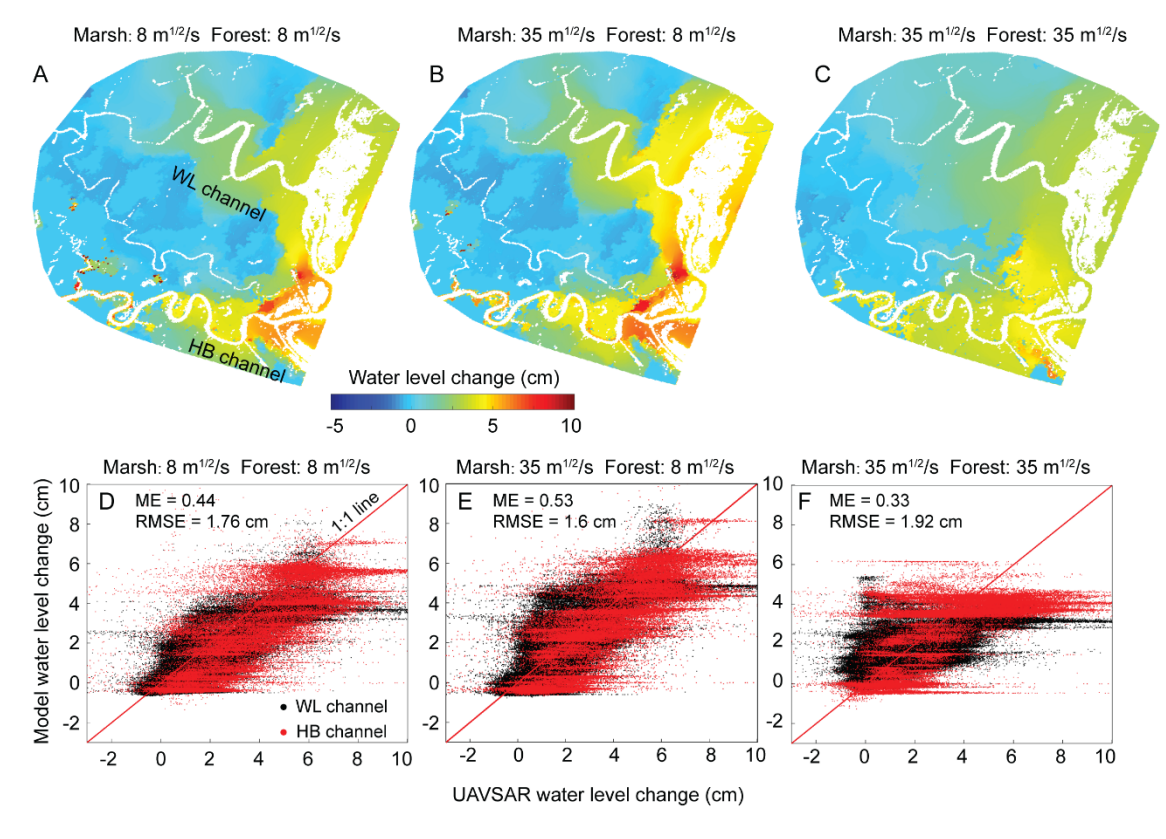


Figure 8. Influence of the bed friction (Chezy's coefficient) of the marsh and forest on water level changes after calibration of river discharge and DTM. (A, D) marsh (8  $m^{1/2}$ /s) and forest (8  $m^{1/2}$ /s), (B, E) marsh (35  $m^{1/2}$ /s) and forest (8  $m^{1/2}$ /s), and (C, F) marsh (35  $m^{1/2}$ /s) and forest (35  $m^{1/2}$ /s). (A, B, C) Spatial distribution of modeled water-level changes, and (D, E, F) the model results as a function of UAVSAR data.

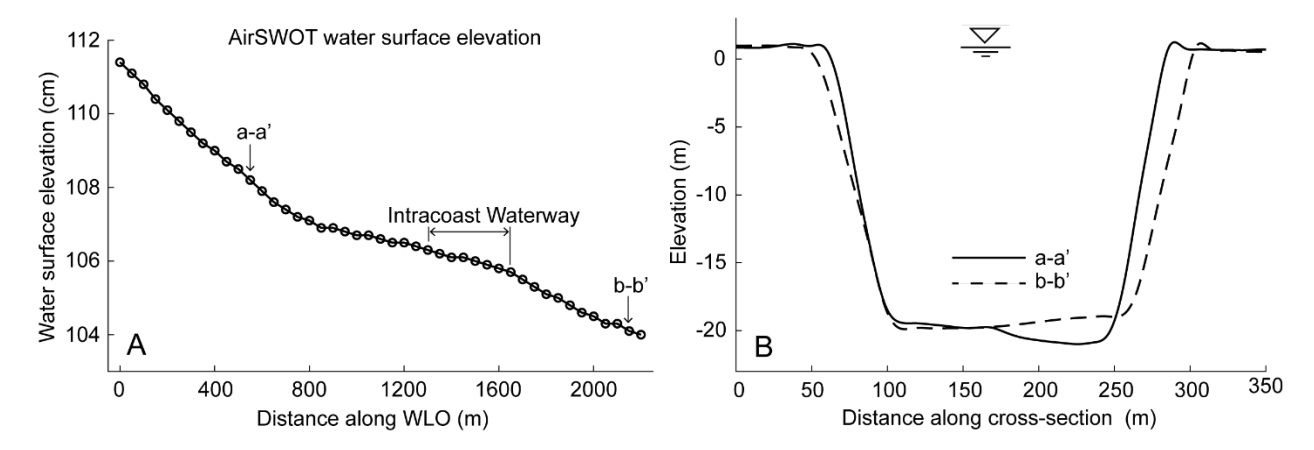


Figure 9. (A) Water surface elevation (NAVD88) measured by AirSWOT along the Wax Lake Outlet (WLO) (Denbina et al., 2019). (B) Bathymetric data of cross sections a-a' and b-b' in Figure 4 used for the calculation of the hydraulic radius.

The slope of the water surface calculated by AirSWOT is presented in Fig. 9A (see also Denbina et al., 2019), while the two cross sections extracted from bathymetric data before and after the GIWW are reported in Fig. 9B. The geometric values of the two cross sections are: A1 = 3945 m<sup>2</sup>,  $R_{h1}$ = 15.40 m, A<sub>2</sub>= 4041m<sup>2</sup>,  $R_{h2}$  = 15.49 m. The bed roughness is assumed to be constant along the WLO (C<sub>1</sub> = C<sub>2</sub>). To reduce possible noise in the AirSWOT data, we calculate the 300-m averaged slope values (S<sub>1</sub>=4.75 cm/km and S<sub>2</sub>=2.25 cm/km), and the 500-m averaged slope values (S<sub>1</sub>=4 cm/km and S<sub>2</sub>=2.33 cm/km, Fig. 9A, see also Denbina et al., (2019)). The corresponding value of Q<sub>2</sub>/Q<sub>1</sub> is 0.71 for the 300-m slope and 0.78 for the 500-m slope, which means that the GIWW receives 29% and 22% of the total river discharge respectively. The calibrated river discharge obtained by reducing of 20% the total discharge at the Calumet station is therefore reasonable, and well accounts for the flow diversion in the intracoastal waterway.

We collected ground-truth elevation data of all the CRMS sites (n=10) within the model domain and compared them to the topographic data used in the model (Figs.4, 10). The averaged positive error is  $12.65 \pm 9.18$  cm for 10 CRMS sites, with a maximum error of 28.43 cm at CRMS-4016. Therefore, ground elevation data indicate a systematic positive error in LiDAR derived elevations. A positive error in the LIDAR elevation of wetlands is very common, and is due to the difficult penetration of the signal in the dense grass canopy (see Rosen et al., 2006).

For the 4 sites (0489, 4779, 4016, 0479) within the UAVSAR area, the DTM correction using our method reduces the error from 20.27 cm to 6.82 cm. The correction little improves the elevation at CRMS-4779 (Fig. 10); this is

probably due to the very small value of water level change measured by UAVSAR (Fig. 4) and the complex network of narrow channels not well represented in the modelling mesh. Despite this, our method seems capable of reducing the elevation error at different locations.

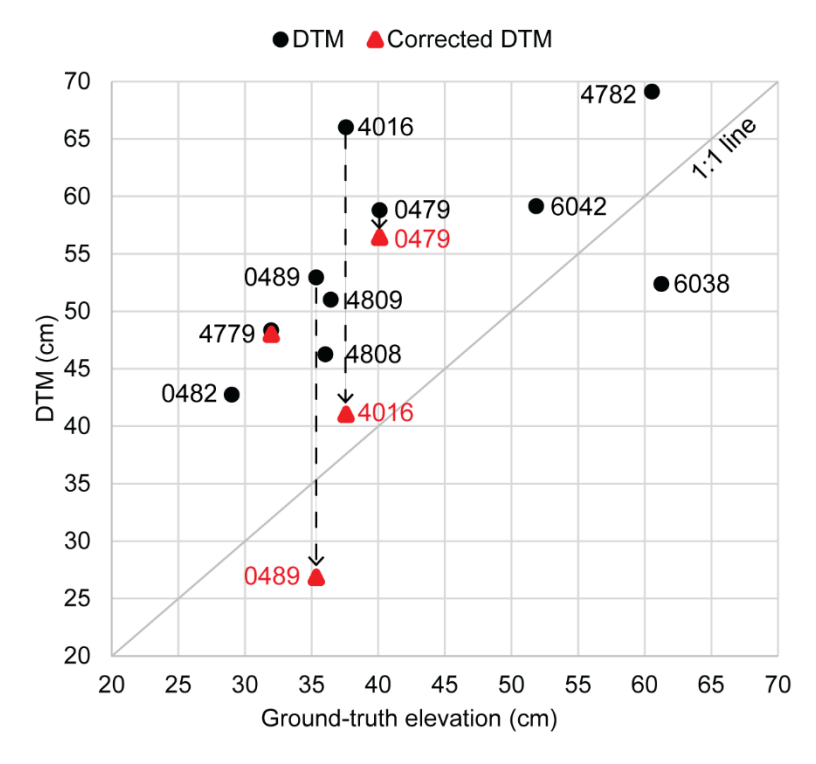


Figure 10. The initial elevations derived from LiDAR data (n=10, indicated as black dots) and corrected elevations based on UAVSAR data (n=4, indicated as red triangle) as a function of ground truth elevations measured at Coastwide Reference Monitoring System (CRMS) sites. See locations of CRMS sites in Fig.4.

### 5. Discussion

UAVSAR repeat-pass interferometry can detect water-level changes beneath vegetation canopies at a time scale of minutes to hours, making it possible to capture tidal propagation in coastal wetlands. The high-spatial-resolution observations of water-level change provided by this sensor can be used to calibrate hydrodynamic models. We developed a high-resolution hydrodynamic model and compared its output with the water-level changes measured by UAVSAR over a 2.5-hour period during which tidal flow caused water level change in channels and adjacent wetlands.

We found that the accuracy of the LiDAR-derived topography and of the river discharge used as a boundary condition are important for the overall model performance, whereas the calibration of bed friction becomes regionally important only with boundary conditions and DTM calibrated.

#### 5.1 Model calibration and measurements uncertainty

A calibrated model should reproduce tidal and riverine fluxes at the boundaries, because very small errors in water levels amplitude and phase can change flow patterns within the model domain (Abbott and Skovgaard, 1978; Cunge, 2003). Pellettier (1987) showed that uncertainty of discharge measurements at river stations could be as high as 20% of the observed value. Calibration of numerical models of natural river streams (e.g. Po River in Italy, Domeneghetti et al., 2012) can produce unrealistic Manning's coefficients, to compensate for the uncertainty of discharge measurements (Horritt and Bates, 2002). In our study area, potential sources of uncertainty include errors in the river discharge at the northern boundary due to interaction of the Wax Lake Outlet with the GIWW, the disconnection with adjacent wetlands east and west of the model domain, and poor spatial information on hydrological connectivity from small-scale creeks (Hiatt and Passalacqua, 2015).

High river floods can attenuate tidal flows, leading to small temporal variations in water level (Sassi and Hoitink, 2013; Van de Kreeke and Brouwer, 2017). As a first step, the incoming river flow is calibrated to yield a comparable instantaneous water-level change at the wetland margin. We found that lowering the river discharge at the boundary does increase variations in water level, particularly in lower marshes, however the overall model performance as measured by the parameters ME and RMSE show little improvement (Fig. 5). The hydrodynamic model performance can be significantly improved with a 2-D spatial comparison with measured water-level changes during a tidal cycle. Correcting the DTM using the measured water-level change had a much larger impact on model performance. It is important to note that the calibration of the wetland DTM and friction coefficient are meaningful only if the correct tidal signal is present at the wetlands margin and at the inlet of the tidal channels.

A summary of previous studies at different sites show that the averaged LiDAR elevation error in salt marshes is 18 cm with a standard deviation of 14 cm. This error is likely to result in misleading hydrodynamic modeling outcomes (Alizad et al., 2020; Buffington et al., 2012). In Wax Lake Delta, we directly refine the wetland DTM by coupling a hydrodynamic model and UAVSAR data. The model performance in terms of water-level changes substantially

improves the DTM adjustment. The high positive LiDAR bias (~ 0.4 m) in the marsh and the low bias in the forest (Fig. 11) indicates the necessity of DTM adjustment especially for marshes, in low-lying micro-tidal coastal deltas. In the forest area (Site 1, in Fig. 11) the average DTM elevation is between 0.4 and 0.6 m (NAVD88 datum, positive values indicate a higher elevation) and the changes in water levels measured by UAVSAR are small (~0.1m in 2.5hr). Our topographic calibration increases the elevations of the platform, but only slightly (less than 0.1m). Interestingly, the correction yields a more uniform topography reducing the size of patches in the original DTM that are probably caused by tree crowns (Fig. 11E). In the marsh area (Site 2, Fig. 11) the elevation of the marsh at the channel banks is unrealistically high (above 0.8 m), likely due to the thick grass canopy that prevents the LiDAR signal from reaching the ground. In the model simulations, these areas are unrealistically dry. Note that the elevations are higher in the marsh than in the forest in the original DTM, in disagreement with studies on vegetation patterns in the delta (Fig. 11J) (Morris et al., 2005). The topographic error is confirmed by the large change in water level (Fig. 11I) that would be impossible in a place with such low water levels. The correction proposed by our methodology reduces the elevations by up to 0.4 m (Fig. 11L), creating a more uniform and realistic topography (Fig. 11K). The correction is more pronounced in the marsh area, which is more prone to LiDAR errors (compare Fig. 11F and 11L). After calibration, the marsh site becomes slightly lower than the forest one (compare Figs.11E and 11K), in agreement with the vegetation zonation of the delta.

411

412

413

414

415

416

417

418

419

420

421

422

423

424

425

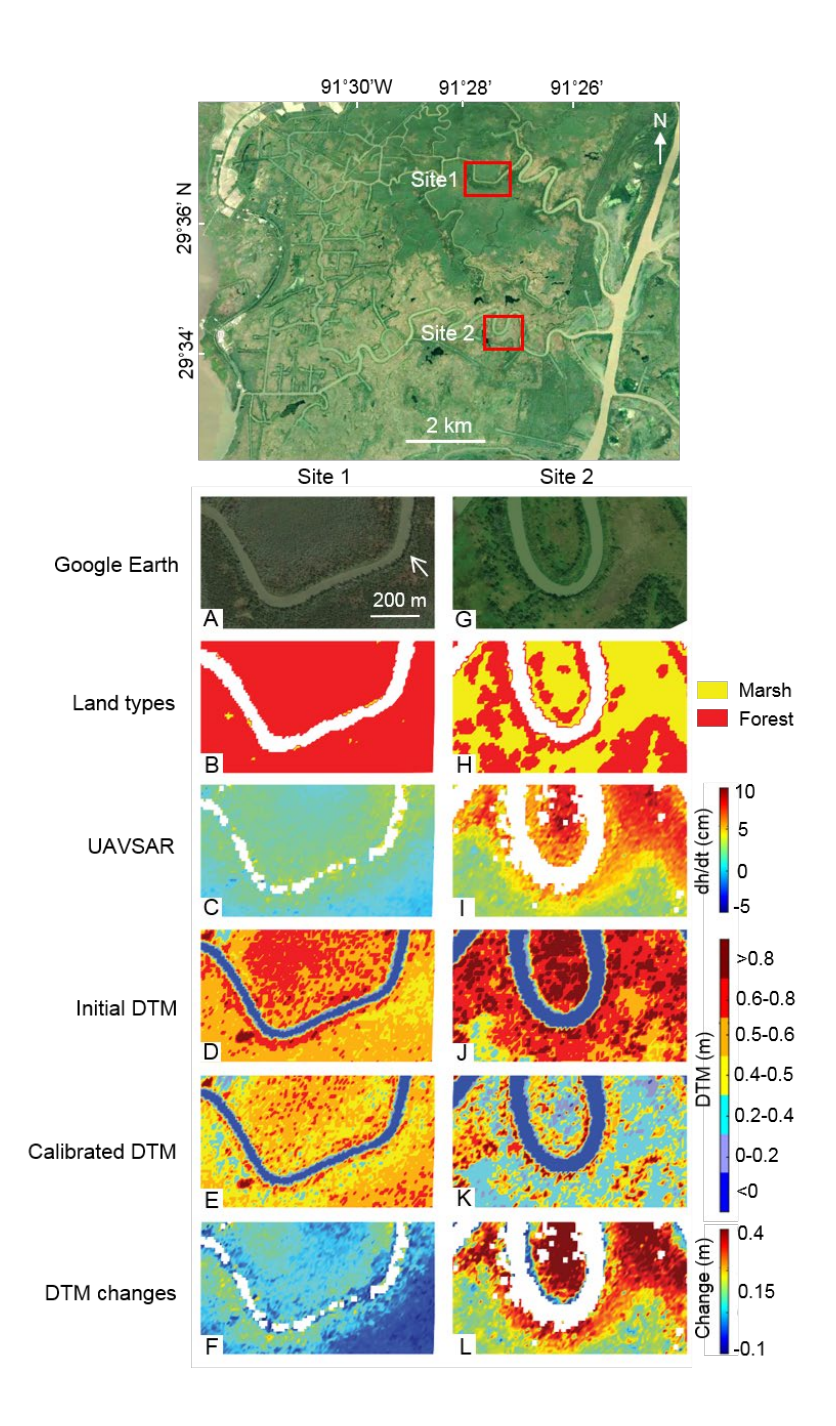


Figure 11. Comparison between Site 1 (forest dominated area near the Wax Lake channel) and Site 2 (marsh dominated area near the Hog Bayou channel). (A, G) Aerial photograph of forest and marsh derived from Google Earth. (B, H) Land classification from Sentinel-2 imagery. (C, H) Water level changes in 2.5hr obtained with UAVSAR. (D, J) Initial DTM (NAVD88, positive values indicate a higher elevation). (E, K) DTM after modification. (F, L) Change in DTM elevations after calibration, positive values indicate a lower elevation.

### 5.2 Limitations of the proposed method

434

435

436

437

438

439

440

441

442

443

444

445

446

447

448

449

450

451

452

453

454

455

456

457

458

459

SAR derived hydraulic variables have already been utilized to calibrate the bed friction of different landscapes, on the assumption that errors in boundary conditions and initial topography have little influence on model results. For instance, the Manning's coefficients of the main channel and floodplains of the Po River in Italy were calibrated with radar altimetry (ERS-2 and ENVISAT water level data) in a 2-D hydraulic model (Domeneghetti et al., 2014). InSAR water-level change data were also used to calibrate the Manning's coefficients in a model of the central Atchafalaya floodplain (Jung et al., 2012). In our system, wetland friction affects the regional water flow, but its calibration did not improve the model performance after the correction of river discharge and topography (Tables 3, 4). This might be because the calibration of discharge and topography contains information of bed friction, and the initial friction setup can mildly influence the accuracy of the calibration of other parameters. Note that the friction coefficients used in the sensitivity analysis cover a very large range (from 8 to 40 m<sup>1/2</sup>/s) and yet they hardly affect ME and RMSE (tables 1,4). Another option would be to keep the wetland elevation constant, and change the friction coefficient locally in an iterative way, as we did for elevation. However, this would lead to very large spatial variations in friction, which are unrealistic for these homogeneous vegetation covers, and friction values very likely outside of the range reported in the literature. Our results are consistent with previous findings suggesting that friction is an inherent physical parameter; therefore, a calibration exclusively based on the adjustment of the friction coefficient could produce unrealistic model results (Cunge.2003). Another possible approach would be to lower or elevate the entire topography of a fixed amount, to correct for possible vegetation biases in the LiDAR data, and then calibrate the friction coefficient. A uniform decrease of 20cm in elevation would increase the flow on the wetland surface, increasing the temporal change in water depth (Fig. S1B), but it would concentrate less flow near the channels, reducing the change in water depth near the HB channel, where UAVSAR data show high values of water level change. On the other hand, a uniform increase in elevation would concentrate the flow in the channels (Fig. S1C), but it would reduce the flow on the wetland surface, with large area completely dry even at high tide. We therefore conclude that the wetland elevation needs to be selectively adjusted as

a function of local hydrodynamic data. This is also evident in Figure 11, which shows higher LiDAR elevations in

the marsh with respect to the forest, when in reality it should be the opposite (the forest is typically located at higher elevations).

In practice, we suggest to set an initial bed friction coefficient for each geomorphic class based on roughness tables, then carefully calibrate boundary conditions and topography based on UAVSAR data, and lastly calibrate bed roughness within a meaningful range. The complexity and nonlinear interactions between different parameters, such as bed friction, elevation and discharge, demand a comprehensive method to optimize the model performance with multiple parameters calibrated simultaneously in a physical way. The topography correction method adjusting elevation at each model cell by the difference in water level changes between model and UAVSAR may have limitations when applied to other systems. 1) The method empirically relates elevation error to water level change, without solving the physical functions between water level change, elevation and friction. 2) Changes in bed elevation at one cell would affect tide propagation and water level changes at cells downstream; therefore the empirical method may produce unrealistic results for a patchy and irregular topography. All the calibrations are based on a sole parameter of water level change derived from UAVSAR, however it is unknown whether this calibration would influence the model performance with respect to other parameters, such as water level and flow velocity. Future research may involve multiple hydraulic parameters for model calibration, e.g. a combination of water level change (UAVSAR) and water surface slope (AirSWOT).

As the water level changes little (~ 10 cm) during this 2.5-hour time window, here we set constant values of bed friction for the marsh and forest, by assuming that it includes the friction caused by vegetation canopy (Zhang et al., 2020). However, hydraulic models in rivers show that the effective friction is proportional to the bed elevation variance and inversely proportional to depth (Rodríguez et al., 2020). Models that require high accuracy can integrate remote sensed vegetation parameters, defining a wetland friction variable in space and time (Fagherazzi et al., 2020). The 2.5-hour UAVSAR campaign was conducted during river flood and high-water levels. When the vegetation is submerged, large-scale sheet flow becomes important, and the relative difference in friction between the channels and platform decreases (Temmerman et al., 2005; Fagherazzi et al., 2012). Similarly, the relative difference in friction between the marsh and forest would also decrease with increasing water depths. Future research can use consecutive UAVSAR observations covering a full tidal cycle to explore the sensitivity of bed friction to different vegetation species and submergence depths.

Our model fails to capture water level variations in the lower HB channel (Fig. 4B) most likely due to the coarse mesh grid resolution that do not fully resolve the small-scale creeks (see area in the red dotted circle in Fig. 6B). A discontinuous channel with a width of one cell does not allow the correct propagation of the tidal and riverine signal, decreasing water fluxes and affecting water levels. As a result, the model performs better in the upper subdomain (WL channel). Future research should evaluate the influence of bathymetric resolution on tidal propagation from the main Wax Lake Outlet to the small creeks. The acquisition time of the UAVSAR data is also important. During low river discharge and neap tides, the calibration can be very challenging due to the small magnitude of water level changes and the limited accuracy of wetting and drying schemes utilized by numerical models. Even during high riverine flow and with the wetlands inundated, the water-level change is only in the range of ~5 cm/hr. For systems with larger tidal ranges (e.g. the Fly River delta, Canestrelli et al., 2010, or the Yangtze delta, Zhang et al., 2018), the large temporal variations in water levels can be more easily detected by UAVSAR, expanding the application of this technology.

#### 6. Conclusions

UAVSAR can detect water level changes beneath vegetation canopies with high spatial and temporal resolution. We presented here the first comparison between UAVSAR observations of tide-induced water level change and numerical simulations with a hydrodynamic model. The following results were obtained from our analysis:

- A comparison between model results and UAVSAR data indicates that small errors in bathymetry (up to 20 cm) have a strong effect on the hydrodynamics of the wetland platform. This result is of general validity for microtidal areas, and was never highlighted before for lack of distributed hydrodynamic data on the marsh platform.
- 2) State-of-the-art topographic data of wetlands obtained for example from LiDAR are therefore inadequate for modeling purposes, because they are often affected by vertical errors in the order of centimeters caused by the dense vegetation cover.
- 3) A correction of the topography is possible by combining UAVSAR data and a high-resolution numerical model that solves the platform hydrodynamics. This coupling is necessary because only a numerical model can convert the hydrodynamic information collected by UAVSAR in elevation.

4) The topographic correction is spatially distributed (resolution of 10 m) and physically based: at every point of the mesh the elevation is improved by iteratively solving the hydrodynamics and comparing it to UAVSAR data. This correction is therefore superior to previous corrections that were either uniform in space (e.g. lowering the marsh of a fixed amount) or based on ancillary data not directly linked to platform hydrodynamics (e.g. vegetation biomass).

In conclusion, our results demonstrate significant improvement in parametrizing a hydrodynamic model. In particular, we were able to correct wetland topography, which traditionally requires labor-intensive campaigns to collect sparse in-situ measurements. We provided a general framework for model calibration that adjusts river discharge and LiDAR-derived wetland topography based on the UAVSAR data. The calibration enables realistic tidal propagation in the wetlands, with the model efficiency improving from 0.15 to 0.53 and the RMSE decreasing by 26%. Our novel approach using airborne remote sensing to calibrate hydraulic variables will substantially improve the reliability and accuracy of model simulations, and thus advance our understanding of hydrodynamics in coastal wetlands.

## Acknowledgements

This work within NASA Delta-X project, is funded by the Science Mission Directorate's Earth Science Division through the Earth Venture Suborbital-3 Program NNH17ZDA001N-EVS3. This work was partly performed by the Jet Propulsion Laboratory, California Institute of Technology, under contract with the National Aeronautics and Space Administration (NASA). S.F was also partially funded by NSF grants DEB-1832221 to the Virginia Coast Reserve Long-Term Ecological Research project and OCE-1637630 to the Plum Island Ecosystems Long-Term Ecological Research project.

#### Reference

- 1. Abbott, M. B., Petersen, H. M., & Skovgaard, O. (1978). On the numerical modelling of short waves in shallow water. Journal of Hydraulic Research, 16(3), 173-204. <a href="https://doi.org/10.1080/00221687809499616">https://doi.org/10.1080/00221687809499616</a>
- 2. Alizad, K., Hagen, S. C., Morris, J. T., Medeiros, S. C., Bilskie, M. V., & Weishampel, J. F. (2016). Coastal wetland response to sea-level rise in a fluvial estuarine system. Earth's Future, 4, 483–497. https://doi.org/10.1002/2016EF000385

Alizad, K., Medeiros, S. C., Foster-Martinez, M. R., & Hagen, S. C. (2020). Model sensitivity to
 topographic uncertainty in meso-and microtidal marshes. IEEE Journal of Selected Topics in Applied Earth
 Observations and Remote Sensing, 13, 807–814. https://doi.org/10.1109/JSTARS.2020.2973490

- 4. Allen, J. I., Somerfield, P. J., & Gilbert, F. J. (2007). Quantifying uncertainty in high-resolution coupled hydrodynamic-ecosystem models. Journal of Marine Systems, 64(1-4), 3-14. https://doi.org/10.1016/j.jmarsys.2006.02.010
  - 5. Alsdorf, D. E., Rodríguez, E., & Lettenmaier, D. P. (2007). Measuring surface water from space. Reviews of Geophysics, 45(2). <a href="https://doi.org/10.1029/2006RG000197">https://doi.org/10.1029/2006RG000197</a>
  - 6. Alsdorf, D., Melack, J., Dunne, T. et al. Interferometric radar measurements of water level changes on the Amazon flood plain. Nature 404, 174–177 (2000). https://doi.org/10.1038/35004560
  - 7. Best, Ü. S., Van der Wegen, M., Dijkstra, J., Willemsen, P. W. J. M., Borsje, B. W., & Roelvink, D. J. (2018). Do salt marshes survive sea level rise? Modelling wave action, morphodynamics and vegetation dynamics. Environmental modelling & software, 109, 152-166. https://doi.org/10.1016/j.envsoft.2018.08.004
  - 8. Buffington, K. J., Dugger, B. D., Thorne, K. M., & Takekawa, J. Y. (2016). Statistical correction of lidar-derived digital elevation models with multispectral airborne imagery in tidal marshes. Remote Sensing of Environment, 186, 616-625. <a href="https://doi.org/10.1016/j.rse.2016.09.020">https://doi.org/10.1016/j.rse.2016.09.020</a>
  - 9. Carle, M. V., Sasser, C. E., & Roberts, H. H. (2015). Accretion and vegetation community change in the Wax Lake Delta following the historic 2011 Mississippi River flood. Journal of Coastal Research, 31(3), 569-587. <a href="https://doi.org/10.2112/JCOASTRES-D-13-00109.1">https://doi.org/10.2112/JCOASTRES-D-13-00109.1</a>
  - 10. Canestrelli, A., Fagherazzi, S., Defina, A. and Lanzoni, S., (2010). Tidal hydrodynamics and erosional power in the Fly River delta, Papua New Guinea. Journal of Geophysical Research: Earth Surface, 115(F4). https://doi.org/10.1029/2009JF001355
  - 11. Center for Operational Oceanographic Products and Services (CO-OPS). 2018. CO-OPS Water Level Data from the Coastal Tide Gauge and Great Lake Water Level Network of the United States and US Territories. NOAA National Centers for Environmental Information. doi:10.25921/dt9g-2p60.
  - 12. Chen, C. W., & Zebker, H. A. (2002). Phase unwrapping for large SAR interferograms: Statistical segmentation and generalized network models. IEEE Transactions on Geoscience and Remote Sensing, 40(8), 1709-1719. https://doi.org/10.1109/TGRS.2002.802453
  - 13. Chow VT. 1959. Open Channel Flow. McGraw-Hill Book Company: Singapore.
  - 14. Cooper, H. M., Zhang, C., Davis, S. E., & Troxler, T. G. (2019). Object-based correction of LiDAR DEMs using RTK-GPS data and machine learning modeling in the coastal Everglades. Environmental modelling & software, 112, 179-191. <a href="https://doi.org/10.1016/j.envsoft.2018.11.003">https://doi.org/10.1016/j.envsoft.2018.11.003</a>
  - 15. Cunge, J. A. (2003). Of data and models. Journal of Hydroinformatics, 5(2), 75-98. https://doi.org/10.2166/hydro.2003.0007
  - 16. De Paiva, R. C. D., Buarque, D. C., Collischonn, W., Bonnet, M. P., Frappart, F., Calmant, S., & Bulhões Mendes, C. A. (2013). Large-scale hydrologic and hydrodynamic modeling of the Amazon River basin. Water Resources Research, 49(3), 1226-1243. <a href="https://doi.org/10.1002/wrcr.20067">https://doi.org/10.1002/wrcr.20067</a>
  - 17. Denbina, M.W., M. Simard, T.M. Pavelsky, A.I. Christensen, K. Liu, and C. Lyon. 2020. Pre-Delta-X: Channel Bathymetry of the Atchafalaya Basin, LA, USA, 2016. ORNL DAAC, Oak Ridge, Tennessee, USA. https://doi.org/10.3334/ORNLDAAC/1807
  - Denbina, M.W., M. Simard, E. Rodriguez, X. Wu, and C. Michailovsky. 2021. Pre-Delta-X: L3 AirSWOT-derived Water Level Profiles, Wax Lake Outlet, LA, USA, 2015. ORNL DAAC, Oak Ridge, Tennessee, USA. <a href="https://doi.org/10.3334/ORNLDAAC/1819">https://doi.org/10.3334/ORNLDAAC/1819</a>
  - 19. Denbina, M., Simard, M., Rodriguez, E., Wu, X., Chen, A., & Pavelsky, T. (2019). Mapping water surface elevation and slope in the mississippi river delta using the AirSWOT Ka-Band interferometric synthetic aperture radar. Remote Sensing, 11(23), 2739. https://doi.org/10.3390/rs11232739
  - 20. Domeneghetti, A., Castellarin, A., & Brath, A. (2012). Assessing rating-curve uncertainty and its effects on hydraulic model calibration. Hydrology and Earth System Sciences, 16(4), 1191. https://doi.org/10.5194/hess-16-1191-2012
  - 21. Domeneghetti, A., Tarpanelli, A., Brocca, L., Barbetta, S., Moramarco, T., Castellarin, A., & Brath, A. (2014). The use of remote sensing-derived water surface data for hydraulic model calibration. Remote sensing of environment, 149, 130-141. <a href="https://doi.org/10.1016/j.rse.2014.04.007">https://doi.org/10.1016/j.rse.2014.04.007</a>
- 594 22. Donatelli, C., Zhang, X., Ganju, N. K., Aretxabaleta, A. L., Fagherazzi, S., & Leonardi, N. (2020). A 595 nonlinear relationship between marsh size and sediment trapping capacity compromises salt marshes' 596 stability. Geology, 48(10), 966-970. https://doi.org/10.1130/G47131.1

597
 598
 598
 599
 590
 23. Fagherazzi, S., Kirwan, M. L., Mudd, S. M., Guntenspergen, G. R., Temmerman, S., D'Alpaos, A., & Clough, J. (2012). Numerical models of salt marsh evolution: Ecological, geomorphic, and climatic factors. Reviews of Geophysics, 50(1). <a href="https://doi.org/10.1029/2011RG000359">https://doi.org/10.1029/2011RG000359</a>

- 24. Fagherazzi, S., Mariotti, G., Leonardi, N., Canestrelli, A., Nardin, W., & Kearney, W. S. (2020). Salt Marsh Dynamics in a Period of Accelerated Sea Level Rise. Journal of Geophysical Research: Earth Surface, 125(8), e2019JF005200. <a href="https://doi.org/10.1029/2019JF005200">https://doi.org/10.1029/2019JF005200</a>
- 25. FitzGerald, D. M., & Hughes, Z. (2019). Marsh processes and their response to climate change and sealevel rise. Annual Review of Earth and Planetary Sciences, 47, 481-517. <a href="https://doi.org/10.1146/annurevearth-082517-010255">https://doi.org/10.1146/annurevearth-082517-010255</a>
- 26. Fore, A. G., Chapman, B. D., Hawkins, B. P., Hensley, S., Jones, C. E., Michel, T. R., & Muellerschoen, R. J. (2015). UAVSAR polarimetric calibration. IEEE Transactions on Geoscience and Remote Sensing, 53(6), 3481-3491. https://doi.org/10.1109/TGRS.2014.2377637.
- 27. Hensley, S.; Lou, Y.; Rosen, P.; Wheeler, K.; Zebker, H.; Madsen, S.; Miller, T.; Hoffman, J.; Farra, D. An L-Band SAR for Repeat Pass Deformation Measurements on a UAV Platform. Proceedings of 2nd AIAA Unmanned-Unlimited System, Technologies and Operating-Aerospace, Land and Sea Conference and Workshop and Exhibit, San Diego, CA, USA, 20 September 2003. https://doi.org/10.2514/6.2003-6619
- 28. Hiatt, M., & Passalacqua, P. (2015). Hydrological connectivity in river deltas: The first-order importance of channel-island exchange. Water Resources Research, 51(4), 2264-2282. https://doi.org/10.1002/2014WR016149
- 29. Hladik, C., & Alber, M. (2012). Accuracy assessment and correction of a LIDAR-derived salt marsh digital elevation model. Remote Sensing of Environment, 121, 224-235. <a href="https://doi.org/10.1016/j.rse.2012.01.018">https://doi.org/10.1016/j.rse.2012.01.018</a>
- 30. Horritt, M. S., & Bates, P. D. (2002). Evaluation of 1D and 2D numerical models for predicting river flood inundation. Journal of hydrology, 268(1-4), 87-99. https://doi.org/10.1016/S0022-1694(02)00121-X
- 31. Jung, H. C., Jasinski, M., Kim, J. W., Shum, C. K., Bates, P., Neal, J.,& Alsdorf, D. (2012). Calibration of two-dimensional floodplain modeling in the central Atchafalaya Basin Floodway System using SAR interferometry. Water Resources Research, 48(7). <a href="https://doi.org/10.1029/2012WR011951">https://doi.org/10.1029/2012WR011951</a>
- 32. Jones, C., M. Simard, and Y. Lou. 2020. Pre-Delta-X: UAVSAR-derived Water Level Change Maps, Atchafalaya Basin, LA, USA, 2016. ORNL DAAC, Oak Ridge, Tennessee, USA. https://doi.org/10.3334/ORNLDAAC/1823
- 33. Lee, H., Yuan, T., Yu, H., & Jung, H. C. (2020). Interferometric SAR for Wetland Hydrology: An Overview of Methods, Challenges, and Trends. IEEE Geoscience and Remote Sensing Magazine, 8(1), 120-135. https://doi.org/10.1109/MGRS.2019.2958653
- 34. Liao, Tien-Hao, Marc Simard, Charles Marshak, and Michael W. Denbina. "Mapping Mangrove Extent and Canopy Height in Gabon Using Interferometric Coherence and Freeman-Durden Decomposition from Lband ALOS/PALSAR-2." AGUFM 2019 (2019): H43N-2273.
- 35. Liao, T. H., Simard, M., Denbina, M., & Lamb, M. P. (2020). Monitoring Water Level Change and Seasonal Vegetation Change in the Coastal Wetlands of Louisiana Using L-Band Time-Series. Remote Sensing, 12(15), 2351. https://doi.org/10.3390/rs12152351
- 36. Lu, Z., & Kwoun, O. I. (2008). Radarsat-1 and ERS InSAR analysis over southeastern coastal Louisiana: Implications for mapping water-level changes beneath swamp forests. IEEE Transactions on Geoscience and Remote Sensing, 46(8), 2167-2184. https://doi.org/10.1109/TGRS.2008.917271
- 37. McCabe, M. F., Rodell, M., Alsdorf, D. E., Miralles, D. G., Uijlenhoet, R., Wagner, W., & Shi, J. (2017). The future of Earth observation in hydrology. Hydrology and Earth System Sciences, 21(7), 3879. <a href="https://doi.org/10.5194/hess-21-3879-2017">https://doi.org/10.5194/hess-21-3879-2017</a>
- 38. Medeiros, S., Hagen, S., Weishampel, J., & Angelo, J. (2015). Adjusting lidar-derived digital terrain models in coastal marshes based on estimated aboveground biomass density. Remote Sensing, 7(4), 3507-3525. <a href="https://doi.org/10.3390/rs70403507">https://doi.org/10.3390/rs70403507</a>
- 39. Morris, J. T., Sundareshwar, P. V., Nietch, C. T., Kjerfve, B., & Cahoon, D. R. (2002). Responses of coastal wetlands to rising sea level. Ecology, 83(10), 2869-2877. <a href="https://doi.org/10.1890/0012-9658(2002)083[2869:ROCWTR]2.0.CO;2">https://doi.org/10.1890/0012-9658(2002)083[2869:ROCWTR]2.0.CO;2</a>
- Morris, J. T., Porter, D., Neet, M., Noble, P. A., Schmidt, L., Lapine, L. A., & Jensen, J. R. (2005).
   Integrating LIDAR elevation data, multi-spectral imagery and neural network modelling for marsh characterization. International Journal of Remote Sensing, 26(23), 5221-5234.
   https://doi.org/10.1080/01431160500219018
- 41. Nardin, W., Edmonds, D. Optimum vegetation height and density for inorganic sedimentation in deltaic marshes. Nature Geosci 7, 722–726 (2014). <a href="https://doi.org/10.1038/ngeo2233">https://doi.org/10.1038/ngeo2233</a>

42. Nepf, H. M., & Vivoni, E. R. (2000). Flow structure in depth-limited, vegetated flow. Journal of Geophysical Research: Oceans, 105(C12), 28547-2855. <a href="https://doi.org/10.1029/2000JC900145">https://doi.org/10.1029/2000JC900145</a>

- 43. Olliver, E. A., Edmonds, D. A., & Shaw, J. B. (2020). Influence of floods, tides, and vegetation on sediment retention in Wax Lake Delta, Louisiana, USA. Journal of Geophysical Research: Earth Surface, 125(1), e2019JF005316. <a href="https://doi.org/10.1029/2019JF005316">https://doi.org/10.1029/2019JF005316</a>
  - 44. Oliver-Cabrera, Talib, and Shimon Wdowinski. "InSAR-based mapping of tidal inundation extent and amplitude in Louisiana coastal wetlands." Remote Sensing 8, no. 5 (2016): 393. https://doi.org/10.3390/rs8050393
  - 45. Pelletier, P. M. (1988). Uncertainties in the single determination of river discharge: a literature review. Canadian Journal of Civil Engineering, 15(5), 834-850. https://doi.org/10.1139/188-109
  - 46. Redfield, A. C. (1972). Development of a New England salt marsh. Ecological monographs, 42(2), 201-237. https://doi.org/10.2307/1942263
  - 47. Reed, D.J., Spencer, T., Murray, A.L. et al. Marsh surface sediment deposition and the role of tidal creeks: Implications for created and managed coastal marshes. J Coast Conserv 5, 81–90 (1999). https://doi.org/10.1007/BF02802742
  - 48. Roberts, H. H., DeLaune, R. D., White, J. R., Li, C., Sasser, C. E., Braud, D., & Khalil, S. (2015). Floods and cold front passages: impacts on coastal marshes in a river diversion setting (Wax Lake Delta Area, Louisiana). Journal of Coastal Research, 31(5), 1057-1068. <a href="https://doi.org/10.2112/JCOASTRES-D-14-00173.1">https://doi.org/10.2112/JCOASTRES-D-14-00173.1</a>
  - 49. Rodriguez, Ernesto, Michael Durand, and Renato Prata de Moraes Frasson. "Observing rivers with varying spatial scales." Water Resources Research 56.9 (2020): e2019WR026476. https://doi.org/10.1029/2019WR026476
  - 50. Rogers, J. N., Parrish, C. E., Ward, L. G., & Burdick, D. M. (2018). Improving salt marsh digital elevation model accuracy with full-waveform lidar and nonparametric predictive modeling. Estuarine, Coastal and Shelf Science, 202, 193-211. https://doi.org/10.1016/j.ecss.2017.11.034
  - 51. Rosen, P. A., Hensley, S., Wheeler, K., Sadowy, G., Miller, T., Shaffer, S., & Madsen, S. (2006, April). UAVSAR: A new NASA airborne SAR system for science and technology research. In 2006 IEEE Conference on Radar (pp. 8-pp). IEEE. https://doi.org/10.1109/RADAR.2006.1631770.
  - 52. Rosso, P.H., Ustin, S.L. and Hastings, A., 2006. Use of lidar to study changes associated with Spartina invasion in San Francisco Bay marshes. Remote Sensing of environment, 100(3), pp.295-306.
  - 53. Sassi, M. G., & Hoitink, A. J. F. (2013). River flow controls on tides and tide-mean water level profiles in a tidal freshwater river. Journal of Geophysical Research: Oceans, 118(9), 4139-4151. https://doi.org/10.1002/jgrc.20297
  - 54. Schuerch, M., Spencer, T., Temmerman, S. et al. Future response of global coastal wetlands to sea-level rise. Nature 561, 231–234 (2018). <a href="https://doi.org/10.1038/s41586-018-0476-5">https://doi.org/10.1038/s41586-018-0476-5</a>
  - 55. Shaw, J. B., Mohrig, D., & Whitman, S. K. (2013). The morphology and evolution of channels on the Wax Lake Delta, Louisiana, USA. Journal of Geophysical Research: Earth Surface, 118(3), 1562-1584. https://doi.org/10.1002/jgrf.20123
  - Straatsma, M. W., & Baptist, M. J. (2008). Floodplain roughness parameterization using airborne laser scanning and spectral remote sensing. Remote Sensing of Environment, 112(3), 1062-1080. https://doi.org/10.1016/j.rse.2007.07.012
  - 57. Sun, W., Ishidaira, H., & Bastola, S. (2012). Calibration of hydrological models in ungauged basins based on satellite radar altimetry observations of river water level. Hydrological Processes, 26(23), 3524-3537. <a href="https://doi.org/10.1002/hyp.8429">https://doi.org/10.1002/hyp.8429</a>
  - 58. Swarzenski, C.M., & Perrien, S.M. (2015). Discharge, suspended sediment, and salinity in the Gulf Intracoastal Waterway and adjacent surface waters in south-central Louisiana, 1997–2008: U.S. Geological Survey Scientific Investigations Report 2015–5132, 21 p., http://dx.doi.org/10.3133/sir20155132.
  - 59. Temmerman, S., Bouma, T. J., Govers, G., Wang, Z. B., De Vries, M. B., & Herman, P. M. J. (2005). Impact of vegetation on flow routing and sedimentation patterns: Three-dimensional modeling for a tidal marsh. Journal of Geophysical Research: Earth Surface, 110(F4). <a href="https://doi.org/10.1029/2005JF000301">https://doi.org/10.1029/2005JF000301</a>
  - 60. Thomas, N., Simard, M., Castañeda-Moya, E., Byrd, K. B., Windham-Myers, L., Bevington, A., & Twilley, R. (2019). High-resolution mapping of biomass and distribution of marsh and forested wetlands in southeastern coastal Louisiana. International Journal of Applied Earth Observation and Geoinformation, 80, 257-267. <a href="https://doi.org/10.1016/j.jag.2019.03.013">https://doi.org/10.1016/j.jag.2019.03.013</a>
  - 61. U.S. Geological Survey, 2016, National Water Information System data available on the World Wide Web (USGS Water Data for the Nation), accessed [June 10, 2012], at URL [http://waterdata.usgs.gov/nwis/].

- 709
   62. van de Kreeke, J., & Brouwer, R. L. (2017). Tidal inlets: hydrodynamics and morphodynamics. Cambridge
   710 University Press.
- 711 63. Wdowinski, S., Hong, S. H., Mulcan, A., & Brisco, B. (2013). Remote-sensing monitoring of tide 712 propagation through coastal wetlands. Oceanography, 26(3), 64-69. <a href="http://www.jstor.org/stable/24862065">http://www.jstor.org/stable/24862065</a>

714 715

716

717

718

719

720

721

722

723

- 64. Wiberg, P. L., Fagherazzi, S., & Kirwan, M. L. (2020). Improving predictions of salt marsh evolution through better integration of data and models. Annual review of marine science, 12, 389-413. https://doi.org/10.1146/annurev-marine-010419-010610
- 65. Yuan, T., Lee, H., & Jung, H. C. (2015). Toward estimating wetland water level changes based on hydrological sensitivity analysis of PALSAR backscattering coefficients over different vegetation fields. Remote Sensing, 7(3), 3153-3183. https://doi.org/10.3390/rs70303153
- 66. Zhang, X., Leonardi, N., Donatelli, C., & Fagherazzi, S. (2020). Divergence of sediment fluxes triggered by sea-level rise will reshape coastal bays. Geophysical Research Letters, 47(13), e2020GL087862. <a href="https://doi.org/10.1029/2020GL087862">https://doi.org/10.1029/2020GL087862</a>
- 67. Zhang, X., Fagherazzi, S., Leonardi, N. and Li, J., (2018). A positive feedback between sediment deposition and tidal prism may affect the morphodynamic evolution of tidal deltas. Journal of Geophysical Research: Earth Surface, 123(11), pp.2767-2783. <a href="https://doi.org/10.1029/2018JF004639">https://doi.org/10.1029/2018JF004639</a>